Hypervelocity Target Dynamics as Seen by Three-Dimensional Markers

R. B. POND*
Johns Hopkins University, Baltimore, Md.

AND

NELSON HSU†
University of Kentucky, Lexington, Ky.

In order to observe the interior deformation and the strain field of a target under hypervelocity impact, cube-shaped copper targets 3 in. and 4 in. on an edge were made with imbedded nickel wires, arranged orthogonally, to serve as three-dimensional markers. One target was indented statically with a $\frac{1}{2}$-in. ball bearing for reference. Measurements of the terminal wire positions, as well as Vickers hardness, on sections of all targets indicated that the flowfields were essentially cylindrically symmetric. Calculations of the finite Lagrangian strain were thus made by using cylindrical coordinates. Comparisons of flowfields, strain invariants, and hardness profiles in the targets and the mass' velocities, and energies of the projectiles show definite qualitative correlations. The flow patterns showed that 1) only a small portion (10% to 30%) of the material that initially occupied the crater site was ejected, i.e., the evacuated volume is much smaller than the crater size, and 2) the outside surface of the lips around the crater was originally the top surface of the target. Thus, instead of being formed like the splashes of a liquid, the lips were formed by the progressive folding over of the surface material by shearing forces and pressure from a subsurface, maximum energy center during the crater expansion.

Introduction

WHEN considering targets deformed by hypervelocity impact, investigators have traditionally used evaluating parameters such as crater volume, target weight loss, and hardness variation under the crater. However, as can be noted in Table 1, a discrepancy generally exists between the evacuated volume calculated from the weight loss and the crater volume. In this comparison the projectile is presumed to remain in the target, although disintegrated, in order to maximize the computed evacuated volume (i.e., the projectile weight is added to the weight lost by the target after firing). Such observations lead to the question, 'Where in the target does the ejected material come from?"

Measurements of hardness or recrystallization grain size provide a fair estimate of the strain energy gradients and perhaps express in the best way possible the total work done in the target. However, such data provide no real insight into the flow mechanisms occurring during the penetration. The models presented by Davies[1] and Rinehart and Pearson[2] propose that the evacuated metal probably comes from a roughly spherical volume residing just below the surface of impact. That the surface material is not part of that evacuated is evidenced in the picture of a crater formed by impact in a laminated wax target shown by Frasier and Korpov.[3] This picture shows that the top surface of the target forms the exterior surface of the lip in the cratering process.

Presented as Paper 69–368 at the AIAA Hypervelocity Impact Conference, Cincinnati, Ohio, April 30–May 2, 1969; submitted May 28, 1969; revision received January 7, 1970. This work was sponsored by the U.S. Army, Ballistics Research Laboratory, Aberdeen Proving Ground, Md., under Contract DA 18-001-AMC-745(X). The authors wish to thank E. Harrison for her painstaking manufacture of the targets used.

* Associate Professor, Department of Mechanics.

† Assistant Professor, Department of Engineering Mechanics.

Development of Targets

Because of the uncertainties as to the actual displacements of material in the target during hypervelocity impact, markers were finitely situated in the target so that after penetration their new positions could be measured and the local displacements thereby documented. The technique of marker placement was carried out by forming copper targets from rectangular plates nominally 3 in. × 3 in. and either $\frac{1}{8}$ in or $\frac{3}{8}$ in. thick. Grooves were cut into the surface of each plate $\frac{3}{8}$ in. (or $\frac{1}{8}$ in. for the thinner plate) on center to a depth that would allow the groove cross section area to be exactly equal to the cross section area of a 0.005 in. nickel wire. In one plate all grooves were parallel on both surfaces. After proper degreasing, these plates were oxidized in an open air furnace. The nickel wires were then wound onto the plate so that each groove contained a straight wire segment. The ends of the wire were held in place on the edges of the plate by means of Duco cement. The plates were then stacked so that in each succeeding block the wire directions were changed by 90° as illustrated in Fig. 1. The effect of this stacking was to produce an orthogonal net for every interface. The ensemble was then placed in a steel plate clamping device and insulated from the steel components by graphite. A load of 100,000 lb was placed on the stack of plates and the steel elements clamped together. Upon removal from the press the clamped target ensemble was packed in loose graphite, placed in a furnace, brought up to 1950°F, and held for approximately 4 hr. Bonding was effected by a Cu–Cu_2O eutectic wetting. At the end of the annealing period the mold was stripped away and the target machined to cubic form with as little metal removed as possible. By simply etching the surface after this last milling operation, the nickel wire ends were delineated and the relative positions on all four faces were measured.

A similar target was prepared without the Cu–Cu_2O eutectic bonding technique but using silver solder instead so

Table 1 Ratio of ejecta volume V_e to crater volume V_c for wire marked tough pitch Cu targets

Target no.	Wire spacing, in.	Impact velocity, m/sec	Impact energy, joule	Maximum ejecta mass, g	V_c, cm³	V_e/V_c
1	0.375	4675	1967	1.25	0.95	0.147
2	0.375	4678	1970	1.96	1.08	0.201
3	0.375	4827	2097	2.26	1.75	0.143
4	0.375	4517	1836	2.17	1.40	0.171
5	0.375	4623	1923	2.29	1.35	0.193
6	0.375	4694	1983	0.91	0.84	0.119
7	0.375	4661	1955	0.94	0.86	0.117
66-3	0.125	4220	9880	5.23	5.84	0.099

that under identical firing conditions the effect of the interface material on the deformation process could be studied. After joining the plates, the targets contained parallel planes of two-dimensional arrays of wires. The wires in any plane intersect to form squares of sides $\frac{3}{8}$ in. or $\frac{1}{8}$ in. (depending on the original groove disp'acement).

Analysis of Targets

After hypervelocity penetration by drill rod projectiles, each target was sectioned through the crater center so that the section was perpendicular to the initial direction of one of the sets of wires that formed the planar arrays. Subsequent lathe cuts (incremental) parallel to this face permitted documentation of the terminal position of this set of wires. In general, only one set of wires in the planar array gives information by this section technique. The terminal positions of the wires were measured using a cathetometer. The accuracy of the measurements was ±0.002 in. The lathe cuts remained within 0.02 in. parallel to the outside surface (opposite to section plane). The origin of the coordinates was chosen to be a corner of the target sufficiently removed from the crater to be undeformed. Obviously, both joining techniques introduce interfaces that may affect the response of the targets to the impact. The use of two joining techniques allowed an examination of the effect of the bond. The axis of impact relative to the stacking of the plates as well as the thickness of the plate containing the impact surface was varied.

Table 2 gives some qualitative information about the cratering of the target as affected by the aforementioned parameters. The following remarks are in order relative to Table 2:

1) S1 and S2 have displacement fields both qualitatively and quantitatively similar.

2) In S3 the top plate was milled to $\frac{3}{16}$ in. nominal thickness. This plate split from the rest of the target upon firing

Table 2 Tough pitch copper targets with wire markers

Target no.	Impact velocity, m/sec	Impact energy E_I, joule	Bond	V_c, cm³	Axis of impact
S1	3190	2232	Cu–Cu_2O	1.355	normal
S2	3220	2285	silver solder	1.373	normal
S3	3120	2142	Cu–Cu_2O	2.537	normal
S4	3150	2175	silver solder	1.443	parallel
S5	3830	3234	Cu–Cu_2O	1.540	parallel
S6	static	50	silver solder	1.088	normal
66-3	4220	9880	silver solder	5.84	normal

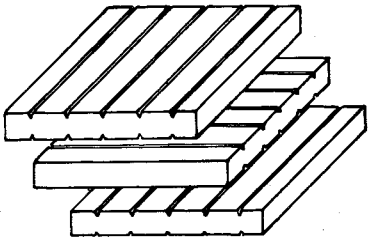

Fig. 1 Stacking of target plates.

and was bent to a convex shape with respect to the axis of the striking projectile. Only the top plate was penetrated. The vertical displacements were larger than that in S1 or S2.

3) S4 has smaller vertical displacements than those in S1 or S2 for the same initial distance from the impact center.

4) Target S5 split along an interface at the center of the crater. Its displacement field is greater in magnitude than those of targets that did not split. However, S5 had a higher impact energy.

5) Target S6 was impressed statically with a steel ball, the impression being 80% of the volume of craters in S1 and S2. The displacement field was of larger magnitude at the same distances from the surface and extended further into the target than in S1 or S2. The total work done in this case was 50 joule. No lip was formed in this annealed "target." In fact, there is a general sinking of material as the indentation was approached.

The following generalizations can be made: The effect of changing the orientation of the plates is greater than the effect of changing the type of bond so long as splitting does not occur. It is felt that the results for S3 indicate a reflection phenomenon of either a tensile release wave from the free surface or a reflected compression wave from the interface. Another possibility of interpretation is bending caused by inertia forces in the flow of material to form the lip.

From the split targets S5 and S3 it was possible to ascribe a maximum volume for the ejected material relative to the undeformed target. This volume, if assumed hemispherical, is less than 30% of the terminal crater volume. This figure agrees quite well with the mass loss measurements on tough pitch copper (see Table 1).

Derivation of the Eulerian and Lagrangian Displacement Fields

Throughout this paper capital letters will designate Lagrangian variables, lower case letters will designate Eulerian variables. The Lagrangian displacement field is given by plots of displacement vs terminal position.

The measurements of all terminal wire positions were plotted for constant cross sections (Fig. 2). The target free surfaces were assumed undeformed, and the initial wire positions were superposed on these plots.

Consideration of the data indicates that one must make some assumption about the symmetry character of the displacement field in order to determine from what initial position points on the terminal line came. Hardness contours and displacement plots indicate that an axis of symmetry passes through the center of the crater perpendicular to the

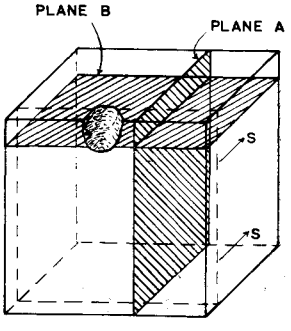

Fig. 2 Orientation of section planes in target (S = sectioning direction).

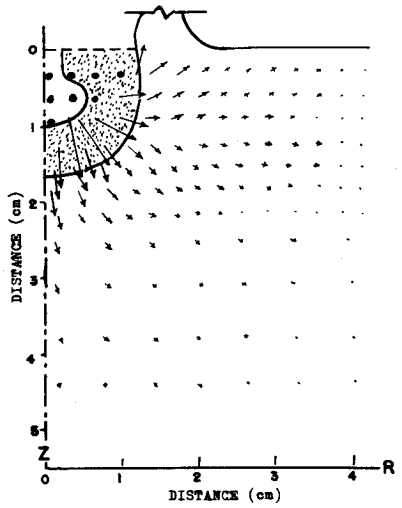

Fig. 3 Vector displacement of flowfield around crater.

impact surface. By presuming cylindrical symmetry, the coordinate system is represented by Z as the distance from the impacted surface and R as the distance from the axis of symmetry. It is then possible to compute or to measure the initial position and the displacement of the wires from the plots. The displacements in the Z direction are designated W and those in the R direction are designated U. Figure 3 indicates the vector displacement from initial position relative to the crater. Figure 4 shows the vertical and horizontal displacement of the wires from initial positions as a function of Z for various values of R.

Figure 5 shows the vertical and horizontal displacement of the wires from initial positions as a function of R for various values of Z. Before calculating the finite Lagrangian strains, note should be made of some approximations and the general character of the flowfield.

Adjacent to the crater surface is a region of reverse flow to form the lip. Wires are observed extending into the lip. In 2S Al targets sectioned and macroetched as fired, grain elongation along the crater wall showed that considerable plastic flow is associated with a region approximately as wide as the maximum lip width. This region has a maximum width of 0.4 cm in the targets examined. A large region of the target (characterized by $R > Z$) has an approximately radial displacement field.

Deformation gradient tensor can be calculated from the displacement functions (of position). If we use polar coordinates, denote R and Z as the horizontal distance from the impact axis and the vertical distance from the top surface,

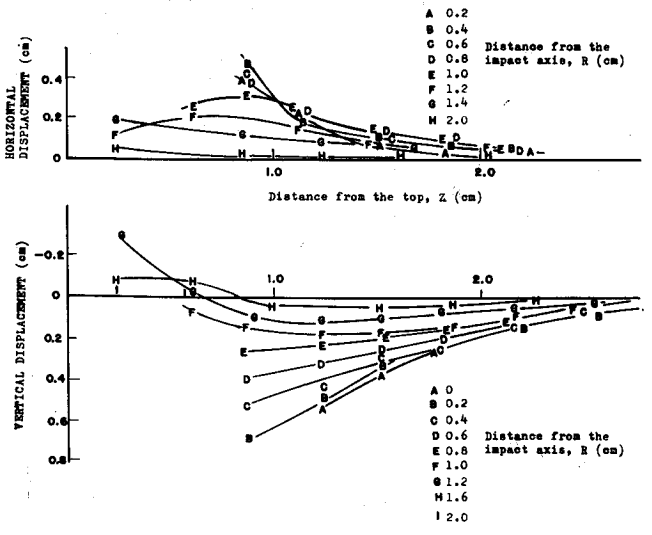

Fig. 4 Horizontal and vertical displacements of wires as a function of Z for various R values.

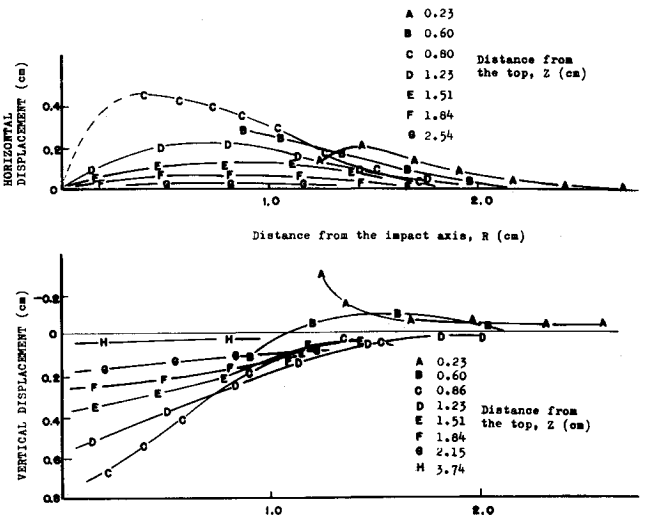

Fig. 5 Horizontal and vertical displacements of wires as a function of R for various Z values.

U and W as the displacements in the R and Z directions, respectively (displacement in the azimuth is zero because of axial symmetry), then the matrix of deformation gradient is

$$[U_{i,j}] = \begin{bmatrix} U_R & 0 & U_Z \\ 0 & 0 & 0 \\ W_R & 0 & W_Z \end{bmatrix}$$

where

$$U_R = \partial U(R,Z)/\partial R, \quad U_Z = \partial U(R,Z)/\partial Z$$
$$W_R = \partial W(R,Z)/\partial R, \quad W_Z = \partial W(R,Z)/\partial Z$$

A choice was made to calculate the finite Lagrangian strain tensor and plot the second invariant as a function of position as seen in Fig. 6. All the calculations are made by the following formula: finite Lagrangian strain tensor

$$\epsilon_{RR} = U_R + \tfrac{1}{2}(U_R^2 + W_R^2)$$
$$\epsilon_{ZR} = \epsilon_{RZ} = \tfrac{1}{2}(U_Z + W_R + U_Z U_R + W_Z W_R)$$
$$\epsilon_{R\phi} = \epsilon_{\phi R} = \epsilon_{\phi Z} = \epsilon_{Z\phi} = 0$$
$$\epsilon_{\phi\phi} = U/R + U^2/2R^2, \quad \epsilon_{ZZ} = W_Z + \tfrac{1}{2}(U_Z^2 + W_Z^2)$$

second invariant

$$\epsilon_{ij}\epsilon_{ij} = \epsilon_{RR}^2 + \epsilon_{ZZ}^2 + \epsilon_{\phi\phi}^2 + 2\epsilon_{RZ}^2$$

It was originally felt that this invariant should be related to the energy absorbed and, hence, to hardness profiles taken on the targets. Such hardness profiles were made (Fig. 7) and were compared with the contour plot of the calculated second invariant. However, it is now felt that the energy absorbed

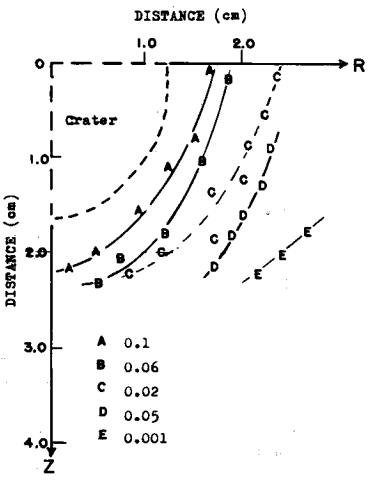

Fig. 6 Plot of the second invariant as a function of crater position.

(or the hardness level) is more likely some function of all three invariants of the strain tensor.

Discussion of Test Results

Ejected Cavitated Volume and Lip Development

Since the geometry of the lips and the crater on hypervelocity targets closely resemble that of the splashes produced when liquid drops impact on liquid, it was believed that the crater was formed by ejecting target material and that the lips were formed during splashing.

Close examination, however, reveals several pieces of information that do not fit this model. First, only a small portion (10% to 30%) of the material that initially occupied the crater site was ejected. Second, the outside surface of the lips of the crater was originally the top surface of the target that flipped over by the shearing force and pressure during the crater expansion. These facts can be shown by the following observations.

1) By weighing the target before and after impact, it was found that the weight lost during impact was far below the calculated number of the crater volume times the density of the target material. A typical case is shown in Table 3. Notice that even by assuming the final weight of the targets contains the whole weight of the projectile, the estimated ejected volume is only 10% of the crater volume.

2) In this example the actual material penetrated by the impact is confined to the first three plates of total thickness 0.86 cm. The final position of all wires but those originally located within 0.8 cm radius of the impact center can be measured. The radius of the crater is about 1.25 cm. These facts also indicate that the ejected volume is much less than the crater volume.

3) A wire originally at the position of the crater was observed extending into the tip of the lip.

4) In 2S Al 3-in. cylindrical targets, elongated grains were developed by the rolling process and were perpendicular to the top surface. The impact direction was parallel to the rolling direction of the cylinder. The target was macro-etched after firing and it was found that the grains remained perpendicular to the outside boundary of the lips.

5) In the case of some targets, the projectile fragmented before hitting the target. Many small craters were formed on the impact surface around the main crater. Some of these small holes were found on the outside (backside) surface of the lips. The explanation of this fact is that they must have been formed before the lips folded back.

6) Instead of forming regular lips around the crater, the top 0.23-cm plate of target Cu–66–3 has been torn into several petal-like forms and flipped over. If the petal-pieces were folded back to the original position, only a small hole of radius less than 0.5 cm would be observable, which, as compared to the 2.5-cm-diam crater, is much smaller.

Based on these observations, it is concluded that the lips were formed during crater expansion by material at the top surface of the target. This plastic deformation cannot be described in terms of hydrodynamic theory.

Table 3 A case of weight lost during impact

Target number	Cu-66-3
Weight before penetration	9451.2 g
Weight after penetration	9443.3 g
Gross weight lost	3.9 g
Projectile weight	1.334 g
Maximum possible weight lost: 3.9 + 1.334 = (assume that the gross weight contains weight of projectile)	5.234 g
Ejected volume (computed)	0.577 cm³
Crater volume (measured)	5.84 cm³

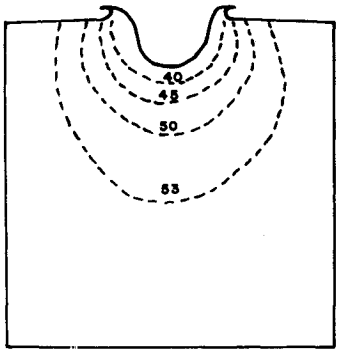

Fig. 7 Plot of hardness contour as a function of crater position in hypervelocity penetrated target S-2.

Symmetry of the Displacement Field

The geometric configuration of a semi-infinite isotropic media under normal impact is always cylindrically symmetric about its impact axis. Sometimes, if the shape of the crater is a hemisphere, one may think that the displacement field around the crater is spherically symmetric. However, the test results of the hardness contours and displacement plots of the 3-in. × 3-in. × 3-in. targets show no spherical symmetry. But an axis of symmetry that passes through the center of the crater perpendicular to the impact surface can be found, i.e., the displacement fields and the hardness contours are essentially symmetric. Thus, the terminal displacement field on any section passing through the symmetry axis of a target will suffice to determine the whole displacement field of the target.

Distribution of the Displacement and the Strain Fields

The displacement of the imbedded wires that can be accurately measured by the cathetometer must be greater than 0.01 cm because the probable error in interpolating the initial wire position is of the order of 0.01 cm. Test results on all hypervelocity impacted targets show that around the impact axis, outside a cylindrical region of radius 2.4 cm and depth 4 cm, no macroscopic displacement can be detected by this technique (i.e., the linear displacement outside the cylindrical region is less than 0.01 cm). Therefore, the strain field calculated from the measured displacement is also confined to the aforementioned region.

Figures 4 and 5 show the displacements as functions of initial positions of target Cu–66–3. The initial positions are represented by R, the distance from the impact axis and Z, the distance from the top surface.

In general, the deformation energy will be a function of deformation gradient. But, if material isotropy is assumed, the deformation energy function will depend on the invariant associated with the deformation gradient only. A plot of the second invariant as a function of terminal position is shown in Fig. 6. As it is compared with the hardness contour plot, a general qualitative agreement is assured.

The hardness profile of a statically impressed target is different from that of a dynamically impacted target as shown by comparing Fig. 7 with Fig. 8. The work hardened region in the center part of the statically impressed specimen (S6)

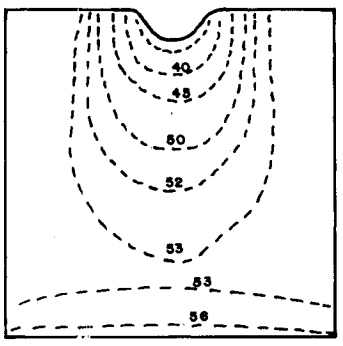

Fig. 8 Plot of hardness contour as a function of crater position in statically penetrated target S-6.

is extended farther down the target. This is in qualitative agreement with the result for the displacement field in the same target, where the displacement is of larger magnitude at the same distance from the surface and the measurable displacements extend farther down than the displacement of all dynamically impacted targets.

Conclusions

It is concluded from these studies that for the targets tested: 1) The ejecta volume was always considerably smaller than the crater volume in hypervelocity penetration; 2) the bulk of the ejecta came from a volume beneath the impact surfaces; 3) the lips of a crater contain the surface of the material originally over the crater; 4) the macroscopic deformation in a statically deformed target is considerably larger than that in a hypervelocity penetrated target of equivalent crater size; 5) the second strain invariant is not completely descriptive of the energy distribution in the target.

References

[1] Davies, R. M., "The Determination of Static and Dynamic Yield Stresses Using a Steel Ball," *Proceedings of the Royal Society*. Ser. A 197, 1949.

[2] Rinehart, J. S. and Pearson, J., *Behavior of Metals Under Impulsive Loads*, American Society for Metals, Cleveland, 1954, pp. 179–202.

[3] Frasier, J. T. and Karpov, B. G., "Hypervelocity Impact Studies in Wax," *Proceedings of the Fifth Symposium of Hypervelocity Impact*, Joint Army, Navy, Air Force, Vol. 1, Pt. 2, 1962 pp. 371–388.

MAY 1970 J. SPACECRAFT VOL. 7, NO. 5

A Reusable System for Deep-Space Exploration

J. G. LAFRAMBOISE* AND G. I. MIDDLETON†
Centre for Research in Experimental Space Science, York University, Toronto, Canada

If nuclear-rocket propellant (hydrogen) can be found on the moon, the proposed reusable deep-space transportation system appears highly attractive for Earth–moon transportation and exploration of the near planets. For planetary missions, powered Earth swingby for departure and return permits system capabilities substantially beyond any previously proposed. The system incorporates new staging techniques that permit complete reuse. Mercury missions use a technique involving an intermediate Venus orbit. If propellant can be found on outer planet moons, exploration of the entire solar system is possible. Transit time to Jupiter is about 10 months. A refueling stop at Jupiter's fifth moon provides shorter transit times to planets beyond than any Jupiter swingby. The system is useful for economical satellite deployment and repair, and for lunar surface transportation. For some missions, ion propulsion may extend system capabilities.

Introduction

REDUCING the cost of manned exploration of the moon and planets appears essential if these bodies are ever to be studied as thoroughly as, for instance, Antarctica. The present cost of placing payload on the lunar surface is ~$30,000/lb ($300 million incremental cost per Saturn 5–Apollo mission for 11,000 lb placed on the moon, i.e. the Lunar Module ascent stage). This is about 60 times the present cost of placing payload in low Earth orbit ($400 to $500/lb for present large launch vehicles). This suggests that lunar mission costs may be reduced more by developing reusable spacecraft to operate from Earth orbit beyond, rather than from the Earth's surface to orbit, as usually envisioned.

Furthermore, we show that a reusable manned deep-space system is feasible in the context of nuclear engine performance and vehicle mass fractions attainable in the immediate future,[1] if usable hydrogen can be found on the moon. Green[2] has cited evidence that suggests that in certain (volcanic) areas, useful amounts of water of crystallization may be expected to exist in the lunar rock, and has studied methods of extracting it. The harsh lunar environment may be expected to remove such water from material near the surface, so its absence in Apollo 11 and 12 samples does not necessarily indicate an absence at greater depths. If such a propellant source becomes available, the subsequent operational cost of transporting a given payload anywhere in the solar system should be only moderately greater than the cost of putting it in orbit. The initial development cost of the proposed system would be substantial, but could be written off at relatively low cost per mission. The system comprises three parts.

Part 1 is a nuclear-powered Deep Space Vehicle (DSV), which would depart from lunar orbit fully fueled, proceed to its planetary or other destination, and return to lunar orbit without discarding any parts. An alternative plan would involve using separate means to insert the DSV into a trans-Earth ellipse and recover it from a translunar ellipse. The crew compartment would be detachable from the rest of the vehicle, which we subsequently refer to as a "DSV propulsion module," and would be capable of remotely controlled operation.

Part 2 is a single-stage Lunar Ascent and Landing Vehicle (LV), to be powered by either nuclear or chemical (hydrogen–oxygen) means, depending on mission requirements and radiation hazards. The LV would be capable of lifting into lunar orbit the DSV crew compartment and propellant supply, docking with the DSV, loading it with propellant, undocking from it, and re-docking with it upon its return. This vehicle would be required to make precisely located landings in order to allow it to be refueled. For maximum flexibility, it would need to be capable of both manned and unmanned operation. It would either wait in lunar orbit for the DSV, or return to the lunar surface until just before its return.

Received October 13, 1969; revision received January 20, 1970.

* Assistant Professor. Member AIAA.
† Research Assistant